

Visualization mitochondrial DNA in living cells under super-resolution microscopy using thiophene-based terpyridine Zn(II) complexes

Yu Shen^{¶a}, Tao Shao^{¶a}, Bin Fang^a, Wei Du^a, Mingzhu Zhang^a, Jiejie Liu^b, Tianyan Liu^b, Xiaohe Tian^{bc*}, Qiong Zhang^{a*}, Aidong Wang^d, Jiaxiang Yang^a, Jieying Wu^a, Yupeng Tian^{a*}

[a] Department of Chemistry, Key Laboratory of Functional Inorganic Material Chemistry of Anhui Province, Anhui University, Hefei 230601, P. R. China.

[b] School of Life Science, Anhui University, Hefei 230601, PR China.

[c] Institute of Physical Science and information Technology, Anhui University.

[d] School of Chemistry and Chemical Engineering, Huangshan College, Huangshan 245041, P.R. China.

[¶]These authors contributed equally to this work.

E-mail address: xiaohe.t@ahu.edu.cn; zhangqiong.314@163.com; yptian@ahu.edu.cn

Materials and apparatus.....	4
Optical measurements.....	4
Synthesis of complex $L_2Zn(PF_6)_2$. (LC).....	4
Synthesis of complex $OL_2Zn(PF_6)_2$. (OLC).....	4
Scheme S1. The synthetic routes for complexes LC and OLC	10
Fig. S1. 1H -NMR spectra and mass spectra of LC and OLC	11
Fig. S2. (a) UV- <i>vis</i> absorption spectra and (b) Fluorescence emission spectra of complexes LC and OLC in DMSO (1.0×10^{-5} M). (c) The photograph of the CIE chromaticity diagrams for complexes LC and OLC in different solvents of complexes LC and OLC (1.0×10^{-5} M). Inset: The fluorescence emission photographs of complexes LC and OLC in Benzene, Dichloromethane, Ethyl Acetate, Acetonitrile, DMSO, DMSO: H ₂ O = 1:1.	11
Fig. S3. (a) (b) UV- <i>vis</i> absorption spectra of complexes LC and OLC in different solvents and (c) (d) Fluorescence emission spectra in different solvents. ($c = 1.0 \times 10^{-5}$ mol/L).	12
Fig. S4. Molecular orbital energy diagrams of complexes LC and OLC	12
Fig. S5. (a) Two-photon cross-sections of LC and OLC in DMSO with $c = 0.8$ mM at the optimal excitation wavelength and (b) Nonlinear optical response of compounds LC and OLC in DMSO at 0.8 mM, obtained under an open aperture Z-scan at 860 nm. Inset: Lippert-Mataga plots for complex LC and OLC	12
Fig. S6. Output fluorescence (I_0) vs. the square of input laser power (I_F) ² at 860 nm for LC and OLC	13
Fig. S7. (a) UV- <i>vis</i> absorption spectra of LC (2 μ M), in the absence and presence of increasing concentrations of ctDNA (0-0.45 μ M) in 50mM Tris-HCl buffer (pH=7.4, 50 mM NaCl). Inset: plots of $[DNA]/(\epsilon_a - \epsilon_f)$ vs. $[DNA]$ and the linear fit line. (b) Fluorescence spectra of EB bound to ctDNA in the presence of LC (0 - 6.4 μ M). $[EB] = 15 \mu$ M, $[DNA] = 15 \mu$ M. The arrows show the intensity changes upon increasing concentrations of the complex. Inset: fluorescence quenching curve of ctDNA-bound EB by LC . (c) The changes in the relative viscosities of ctDNA, EB and Hoechst with increasing concentrations of LC in buffer 50 mM NaCl. The total concentration of ctDNA is 50 μ M. (d) Circular dichroism spectra of ctDNA in the absence (DNA alone) and presence of LC . (e) 1H NMR spectral change of LC in the absence and presence of ctDNA in DMSO- d_6 solution.	13
Fig. S8. UV- <i>vis</i> absorption spectra of OLC (2 μ M) in the absence and presence of increasing concentrations of ctDNA (0-0.45 μ M) in 50mM Tris-HCl buffer (pH = 7.4, 50 mM NaCl). Inset: plots of $[DNA]/(\epsilon_a - \epsilon_f)$ vs. $[DNA]$ and the linear fit line.....	14
Fig. S9. Fluorescence intensity of LC (20 μ M), in the presence of various relevant analytes in Tris-HCl buffer (pH=7.4, 50 mM NaCl) at 37 $^{\circ}$ C.....	14
Fig. S10. Models obtained after molecular modeling of the interaction of LC with DNA (left) and RNA (right).	15
Fig. S11. Time evolution of UV- <i>vis</i> absorption spectra (left) and Fluorescence emission spectra (right) of complex LC in PBS buffers.	15
Fig. S12. The 1H NMR spectra of complex LC in 90% D ₂ O/10% DMSO- d_6 at various time points. The spectra were recorded at 300 K.....	15
Fig. S13. Cytotoxicity data results obtained from the MTT assay.....	16

Fig. S14. Two-photon fluorescence images, Bright field images and Merge images of live MCF-7 cells, A549 cells, HeLa cells and RAW cells stained with LC (10 μ M, λ_{ex} = 840 nm, λ_{em} = 500-600 nm). Scale bar: 20 μ m.	16
Fig. S15. Colocalization experiments involving LC (10 μ M) and Lyso Tracker in HepG2 cells. Scale bar: 20 μ m.	17
Fig. S16. HepG2 cells stained by complex LC after being fixed by paraformaldehyde. Scale bar: 20 μ m.	17
Fig. S17. Photo-stability of LC of confocal and STED imaging.	17
Table S1. Crystal data collection and structure refinement of LC	17
Table S2. Selected Bond Lengths (\AA) and Bond Angles ($^{\circ}$) of LC	18
Table S3. The photophysical data of complex LC and OLC in different solvents.	18
Table S4. Two photon absorption data for LC and OLC	19
Table S5. Calculated leaner absorption properties (nm), excitation energy (eV), oscillator strengths and major contribution for LC and OLC	20
References	20

Materials and apparatus

All chemicals and solvents were dried and purified by standard methods. IR spectra (4000–400 cm^{-1}) were recorded on a Nicolet FT-IR 870 SX spectrophotometer with KBr pellets. The ^1H NMR and ^{13}C NMR spectra were recorded with a Bruker Avance 400 MHz spectrometer (TMS as internal standard in NMR). MALDI-TOF mass spectra were recorded on a Bruker Autoflex III Smartbeam. The UV-visible absorption spectra of dilute solutions were recorded using a SHIMADZU UV-3600 spectrophotometer using a quartz cuvette with a 1 cm path length. One-photon fluorescence spectra were obtained using a HITACHI F-7000 spectrofluorimeter equipped with a 450 W Xe lamp. The concentration of the sample solution was 1.0×10^{-5} mol/L.

Optical measurements

Synthesis of complex $\text{L}_2\text{Zn}(\text{PF}_6)_2$. (LC)

A solution of L^9 (0.48 g, 1 mmol) in dichloromethane-methanol (5 mL-15 mL) was mixed with $\text{Zn}(\text{PF}_6)_2$ (0.18 g, 0.5 mmol) in methanol (5 mL). The reaction mixture was refluxed for 4 h. The mixture was cooled to room temperature and filtered. An orange product was crystallized from methanol and dried under vacuum. Orange powder was obtained. 0.21 g, Yield: 40 %. ^1H -NMR (400 MHz, d_6 -DMSO, ppm): δ 8.74 (d, $J = 4.1\text{Hz}$, 4 H), 8.63 (d, $J = 7.9\text{Hz}$, 4 H), 8.50 (s, 4 H), 8.02 (t, $J = 7.8\text{Hz}$, 4 H), 7.78 (d, $J = 3.6\text{Hz}$, 2 H), 7.55 – 7.48 (4 H, m), 7.41 (t, $J = 7.6\text{Hz}$, 8 H), 7.20 (d, $J = 29.6\text{Hz}$, 16 H), 6.66 (d, $J = 3.6\text{Hz}$, 2 H). FT-IR (KBr, cm^{-1}): 3418, 2917, 1600, 1572, 1548, 1488, 1473, 1439, 1378, 1224, 1159, 1075, 1022, 896, 790, 748, 698, 640, 517. MALDI-TOF-MS: 1028.31.

Synthesis of complex $\text{OL}_2\text{Zn}(\text{PF}_6)_2$. (OLC)

The complex **OLC** was prepared according to the similar procedures with the complex **LC**, except **L** was replaced by **OL**.⁹ Brown powder was obtained. 0.27 g. Yield: 45 %. ^1H -NMR (400 MHz, d_6 -DMSO, ppm): δ 9.02 (d, $J = 8.0$ Hz, 4H), 8.83 (s, 4H), 8.32 (d, $J = 3.4$ Hz, 2H), 8.19 (t, $J = 7.6$ Hz, 4H), 7.87 (d, $J = 4.1$ Hz, 4H), 7.49 – 7.42 (m, 4H), 7.34 (d, $J = 8.6$ Hz, 8H), 7.04 (d, $J = 8.6$ Hz, 8H), 6.41 (d, $J = 3.8$ Hz, 2H), 4.07 (q, $J = 6.8$ Hz, 8H), 1.36 (t, $J = 6.9$ Hz, 12H). ^{13}C -NMR (100 MHz, d_6 -DMSO, ppm): δ 161.37, 156.66, 148.83, 147.77, 141.02, 139.05, 127.43, 126.99, 123.70, 123.26, 116.40, 115.65, 63.36, 14.66. FT-IR (KBr, cm^{-1}): 3437, 2926, 2550, 1796, 1606, 1545, 1505, 1468, 1441, 1381, 1244, 1176. MALDI-TOF-MS: 1205.47.

X-ray crystallography

Single-crystal X-ray diffraction measurements were carried out on a Bruker Smart 1000 CCD diffractometer equipped with a graphite crystal monochromator situated in the incident beam for data collection at room temperature. The determination of unit cell parameters and data collections were performed with Mo-K α radiation ($\lambda = 0.71073 \text{ \AA}$). Unit cell dimensions were obtained with least-squares refinements, and all structures were solved by direct methods using SHELXL-97 program package.¹ All non-hydrogen atoms were refined anisotropically. The hydrogen atoms were added theoretically and riding on the concerned atoms. The final refinement was performed by full-matrix least-squares methods with anisotropic thermal parameters for non-hydrogen atoms on F².

Fluorescence lifetime

For time-resolved fluorescence measurements, the fluorescence signals were collimated and focused onto the entrance slit of a monochromator with the output plane equipped with a photomultiplier tube (HORIBA HuoroMax-4P). The decays were analyzed by ‘least-squares’. As shown in Table S3, the lifetime of **OLC** in DMSO is longer than **LC**, it may be attributed to the electron-based reduction of the nonradiative transition.

Computational details

Optimizations were performed on B3LYP [LANL2DZ] without any symmetry restraints, and the TD-DFT {B3LYP[LANL2DZ]} calculations were carried out with the crystal structure or the optimized structure. All calculations, including optimizations and TD-DFT, were performed using the G09 software. Geometry optimization of singlet-singlet excitation energies were carried out with a basis set composed of 6-31G(d) for C N O H atoms, and the LANL2DZ basis set for Zn atoms. The basis set was downloaded from the EMSL basis set library. The lowest 25 spin-allowed singlet-singlet transitions were taken into account in the calculation of the absorption spectra. All calculations were performed by the use of the Gaussian 03 suite of programs.²

Commission Internationale de l’Eclairage (CIE) chromaticity coordinates

The fluorescence properties are illustrated by the CIE (CIE = Commission Internationale de l’Eclairage) chromaticity coordinates of the emission spectra in Fig. S2c. From the CIE chromaticity diagram, it is cleared that the photoluminescent band of **LC** is located in the blue and green-light region. There is some part located in the yellow-light region as well. The photoluminescent band of **OLC** is almost located in the yellow and green-light region. From the

inset in Fig. S2c, we can see the change of the solvents with increasing polarity of the solvent. **LC** and **OLC** show great sensitivities to each solvent, which could be useful when applied to the development of efficient sensors for the detection of volatile organic compounds (VOCs).³

NLO measurements

Two techniques were used to measure 2PA cross-sections, namely, two-photon excited fluorescence (2PEF) and Z-scan methods. The 2PA cross-sections (σ) were measured using the 2PEF method with the following equation:⁴

$$\sigma = \sigma_{ref} \frac{\Phi_{ref}}{\Phi} \frac{c_{ref}}{c} \frac{n_{ref}}{n} \frac{F}{F_{ref}} \quad (1)$$

Here, the subscript ref stands for the reference molecule. σ is the 2PA cross-section value, c is the concentration of the solution, n is the refractive index of the solution, F is the integrated area of the detected two-photon-induced fluorescence signal, and Φ is the fluorescence quantum yield. The σ_{ref} value of reference was taken from the literature.⁵ The 2PA coefficient β and 2PA cross-sections of σ were measured by the open Z-scan technique.⁶

To study the third-order NLO properties of **LC** and **OLC**, their nonlinear 2PA coefficient (β) and the molecular 2PA cross-sections (σ) were obtained by an open-aperture Z-scan technique using a femtosecond laser pulse (680-1080 nm, 80 MHz).⁶ The pulse length was 140 fs, the thermal heating of the sample with high repetition rate laser pulse was removed by the use of a mechanical chopper running at 10 Hz, and the average laser power was 36 mW. The sample in DMSO (its thickness is 1 mm) was put in the light path, and all measurements were carried out at room temperature. The filled squares represent the experimental data, and the solid line is the theoretical curve modified from the following equations:

$$T(z, s = 1) = \sum_{m=0}^{\infty} \frac{[-q_0(z)]^m}{(m+1)^{3/2}}, \quad q_0(z) = \frac{\beta I_0 L_{eff}}{1+x^2}$$

where $x = z/z_0$, in which $z_0 = \pi\omega_0^2/\lambda$ is the diffraction length of the beam, where ω_0 is the spot size at the focus, λ is the wavelength of the beam, and z is the sample position. I_0 is the input intensity at the focus $z = 0$ and equals the input energy divided by $\pi\omega_0^2$. $L_{eff} = (1 - e^{-\alpha L})/\alpha$ is the effective length, in which α is the linear absorption coefficient and L is the sample length. The 2PA two-photon cross-section (σ_{max}) of **OLC** (252.06 GM) is larger than complex **LC** (227.35 GM) at 860 nm. As shown in Table S4, two-photon absorption cross-section values of **LC** and **OLC** are 2269.75

GM and 2418.29 GM, exhibiting in the order of **OLC** > **LC**. It had been proposed that strong donors within the symmetric molecules could enhance the ICT effect, bringing a large breaking of the alternate symmetry causing an enhancement of the transition dipole moment between excited states which could result in large 2PA activity.

Lippert–Mataga plot.

The Lippert-Mataga equation is the most widely used equation to evaluate the dipole moment changes of the dyes with photoexcitation:⁷

$$\Delta\nu = \frac{2\Delta f}{4\pi\epsilon_0\hbar c a^3} (\mu_e - \mu_g)^2 + b \quad (1)$$

$$\Delta f = \frac{\epsilon - 1}{2\epsilon + 1} - \frac{n^2 - 1}{2n^2 + 1} \quad (2)$$

in which $\Delta\nu = \nu_{\text{abs}} - \nu_{\text{em}}$ stands for Stokes' shift, ν_{abs} and ν_{em} are absorption and emission (cm^{-1}), \hbar is the Planck's constant, c is the velocity of light in vacuum, a is the Onsager radius and b is a constant. Δf is the orientation polarizability, μ_e and μ_g are the dipole moments of the emissive and ground states, respectively, and ϵ_0 is the permittivity of the vacuum. $(\mu_e - \mu_g)^2$ is proportional to the slope of the Lippert-Mataga plot. Only the data involving the aprotic solvents are shown because application of this analysis with solvents where specific solute-solvent interactions are present is not appropriate. As shown in inset of Fig. S5b, the Lippert-Mataga plot of **OLC** gave larger slope than **LC**, which infers larger dipole moment changes for **OLC** with photoexcitation.⁷ The slope of the best-fit line is related to the dipole moment change between the ground and excited states ($\mu_e - \mu_g$). The slopes of two lines are 1776 cm^{-1} for **LC** and 1852 cm^{-1} for **OLC**, respectively. Plots of the Stokes' shifts as a function of the solvent polarity factor Δf is shown in inset of Fig. S5b. The values of $\mu_e - \mu_g$ were calculated as 9.35 D for **LC** and 10.59 D for **OLC**, respectively. The large values of complex **OLC** indicate that the molecules in the excited state have an extremely polar structure. The results of calculated $\mu_e - \mu_g$ values are in good agreement with their nonlinear optical properties (inset of Fig. S5b).

Extraction of mtDNA

The mtDNA used in all vitro experiments was extracted from HepG2 cells according to the instructions of mitochondrial DNA extraction kits, and then stored at zero degree for later use.

Molecular docking with DNA and RNA

Molecular docking techniques are valuable tools in understanding the nature of DNA interaction for the molecule design and the mechanistic study, Fig. 1g and Fig. S10. The crystal structure of DNA (ID:5IP8,CCGGAGCCGG/CCGGCTCCGG) and RNA (ID:5TDK,CCGGCGCCGG/CCGGCGCCGG) were retrieved from PDB database,⁸ explicit hydrogen atoms were added, and all water molecules were then deleted. The structure of DNA and RNA were processed. The active-site cavities of DNA and RNA is defined using the biggest cavity of the surface of RNA and DNA. Docking was carried out using the docking method of ligandfit vina software (version 2016, The Biovia Co.). The parameter was set as default. At the meantime, the binding energy is calculated. CDOCK ENERGY of LC and DNA (-478.775 kJ/mol) fragment was slightly smaller than that of LC and RNA fragment (455.217 kJ/mol), suggesting LC had a more stable interaction with DNA.

Cytotoxicity assays in cells

The study of the effect of LC on viability of HepG2 cells was carried out using the methylthiazolyldiphenyl-tetrazolium bromide (MTT) assay. Prior to treatment with the compound, the growth medium was refreshed, and complex LC was first dissolved in DMSO to 1 mM and then diluted twice with the DMEM cell culture medium to obtain the final concentrations. HepG2 cells were grown to ~70 % confluence in 96-well plates before treatment. They were then incubated at 37 °C in 5 % CO₂ for 24 h before cell viability was measured by the MTT assay. The cell medium solutions were exchanged by 100 mL of fresh medium, followed by the addition of 20 mL (5 mg/mL) MTT solution to each well. The cell plate was then incubated at 37 °C in 5 % CO₂ for 4 h. Absorbance was measured at 570 nm. The absorbance measured for an untreated cell population under the same experimental conditions was used as the reference point to establish 100 % cell viability. Duplicated experiments have been tested.

Cell image

HepG2 cells, MCF-7 cells, A549 cells, HeLa cells and RAW cells were seeded in 24-well glass bottom plate at a density of 2×10^4 cells per well and grown for 96 h. For live cell imaging, cell cultures were incubated with the complexes (10 % PBS: 90 % cell media) at concentration 10 μ M and maintained at 37 °C in an atmosphere of 5 % CO₂ and 95 % air for incubation times ranging for 30 min. The cells were then washed with PBS (3×1 mL per well) and 1 mL of PBS was added to each well. The cells were imaged using confocal laser scanning microscopy using oil immersion

lenses.

For transmission electron microscopy (TEM), cell samples were received pelleted in Eppendorf tubes. HepG2 cells were incubated with complex LC (30 min) and then fixed in 3 % glutaraldehyde and dehydrated in ethanol. The sections were examined using a FEI Tecnai Transmission Electron Microscope at an accelerating voltage of 80 kV. Electron micrographs were taken using a Gatan digital camera.

Confocal microscopy

Confocal microscopy imaging was acquired with a Carl Zeiss LSM 710 confocal microscopy and 63X/100X oil-immersion objective lens using 405nm laser (30% power), with 1024*1024 pixel and *100 scanning speed. The number of scans per line/pixel were 4. Image data acquisition and processing were performed using Zeiss LSM Image Browser, Zeiss LSM Image Expert and Image J.

Stimulated emission depletion (STED) nanoscopy:

STED nanoscopy experiments were performed under Leica DMI8 confocal microscopy equipped with Leica TCS SP8 STED-ONE unit and the compound was excited under STED laser, the emission signals were collected using HyD reflected light detectors (RLDs). Specimen living cells were prepared using similar method as standard confocal microscopy described previously, and donut laser used in 595nm STED laser (70% power), with 2048*2048 pixel and *100 scanning speed and four times per line/pixel. The STED micrographs were further processed 'deconvolution wizard' function using Huygens Professional software (version: 16.05) under authorized license. The area radiuses were estimated under 0.02 micros with an exclusion of 100 absolute background values. Maximum iterations were 40-time, signal-to-noise ration 20 was applied, with quality threshold 0.05; iteration mode: Optimized; Brick layout: Auto.

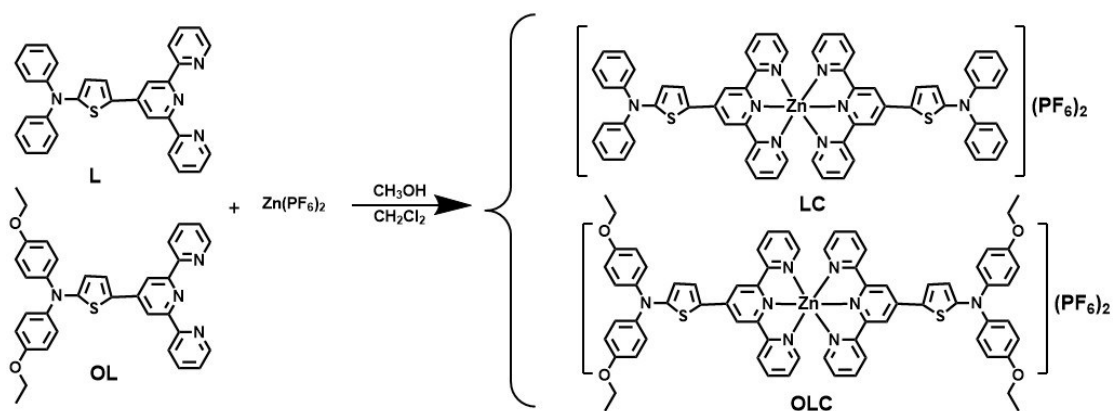
Cellular uptake and distribution (ICP-MS)

To quantify the levels of iridium in different subcellular compartments, ICP-MS was employed. Exponentially growing HepG2 cells were cultured in 25 cm² culture plates treated with the zinc(II) complexes at a concentration of 10 μM for 1 h. After digestion, HepG2 cells were counted and divided into two equal parts for the extraction of the cytoplasm and mitochondria by using a mitochondrial isolation kit, respectively. LC was digested by 60 % HNO₃ at room temperature for 24 h. Each sample was diluted with Milli-Q water to achieve a final volume of 10

mL containing 3 % HNO₃. The concentration of zinc in the three domains was determined by using an inductively coupled plasma mass spectrometer (Thermo Fisher Co., Ltd.).

DNase treatment and CCCP test

For DNase digest test, two sets of living HepG2 cells were stained with 15 μM LC in PBS (pH = 7.4) for 30 min. After washing with PBS twice, a total 1 mL PBS (as control experiment) was added into a set of cells and 25 mg/mL RNase-Free DNase was added into the other set of cells, and then two sets of cells were incubated at 37 °C in 5 % CO₂ for 2 h. In addition, the DNase digest test of cells stained with 30 μM LC was also carried out for comparison. Carbonyl cyanide m-chlorophenylhydrazone (CCCP) can collapsed mitochondrial membrane potential. Mito-deep red, whose uptake was dependent on the mitochondria membrane potential, was inconsistent in the absence or presence of CCCP. CCCP test was carried out to confirm that whether the mitochondria-targeting properties was dependent of the membrane potential.



Scheme S1. The synthetic routes for complexes LC and OLC.

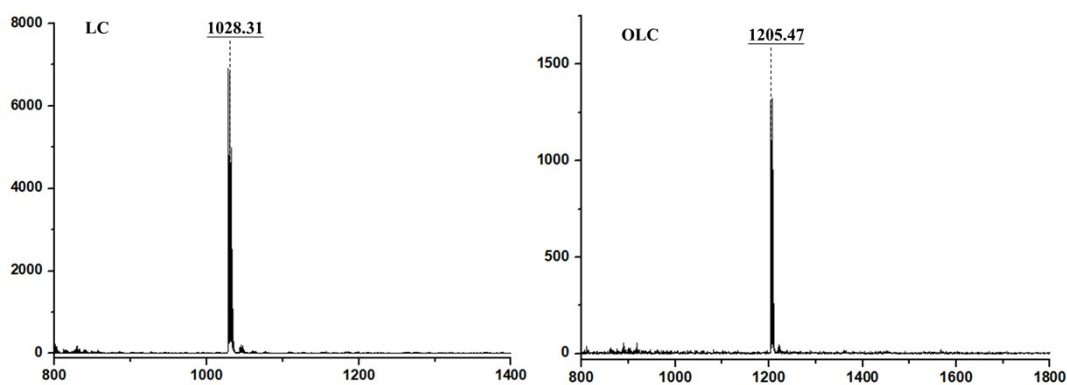
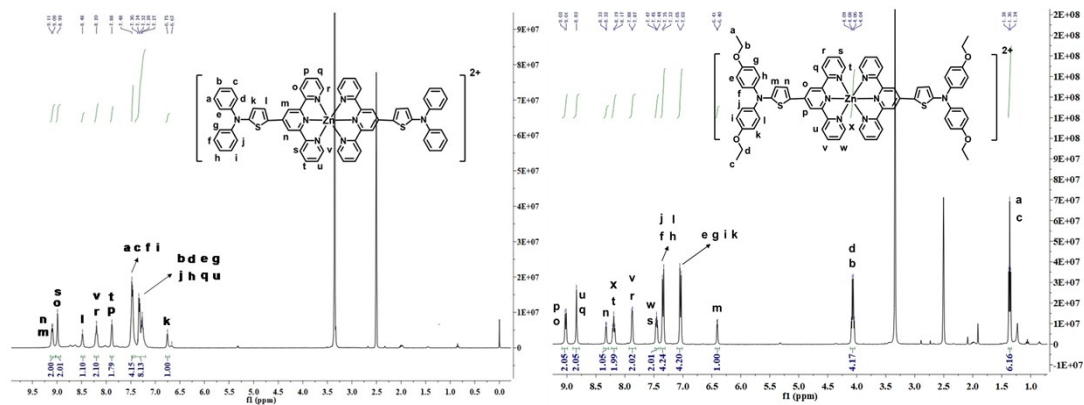


Fig. S1. $^1\text{H-NMR}$ spectra and mass spectra of LC and OLC.

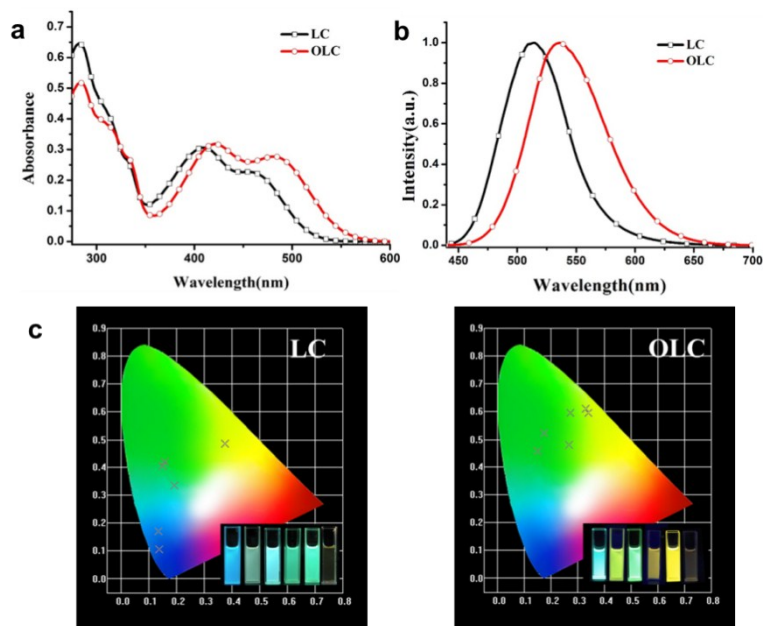


Fig. S2. (a) UV-*vis* absorption spectra and (b) Fluorescence emission spectra of complexes LC and OLC in DMSO (1.0×10^{-5} M). (c) The photograph of the CIE chromaticity diagrams for complexes LC and OLC in different solvents of complexes LC and OLC (1.0×10^{-5} M). Inset: The fluorescence emission photographs of complexes LC and OLC in Benzene, Dichloromethane, Ethyl Acetate,

Acetonitrile, DMSO, DMSO: H₂O = 1:1.

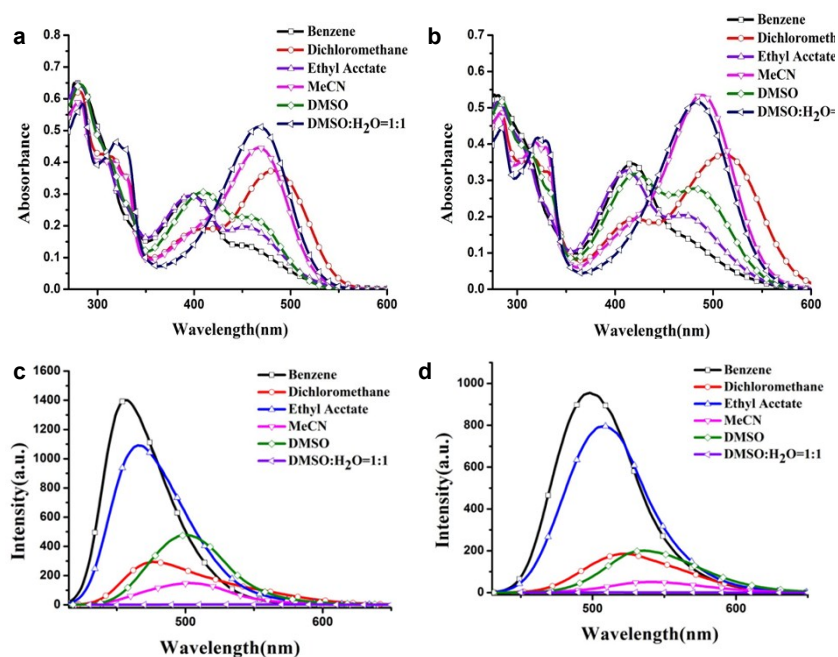


Fig. S3. (a) (b) UV-*vis* absorption spectra of complexes **LC** and **OLC** in different solvents and (c) (d) Fluorescence emission spectra in different solvents. ($c = 1.0 \times 10^{-5} \text{ mol/L}$).

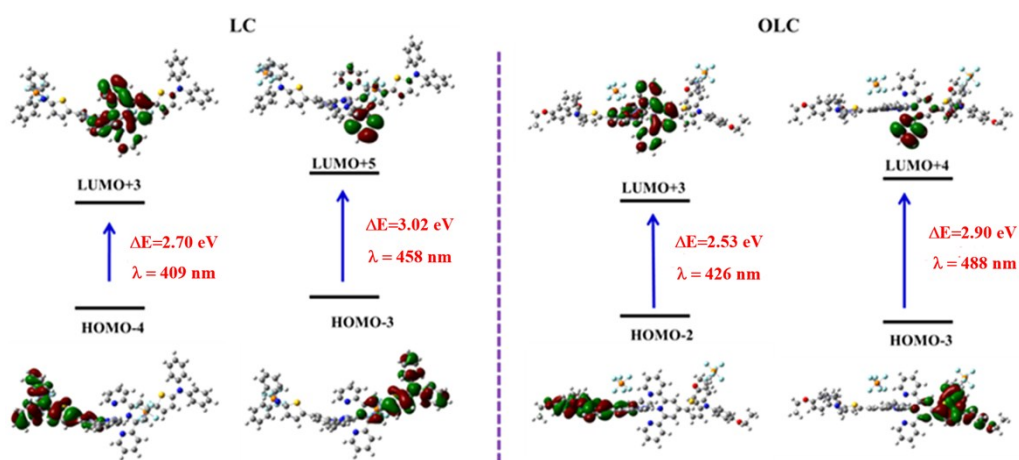


Fig. S4. Molecular orbital energy diagrams of complexes **LC** and **OLC**.

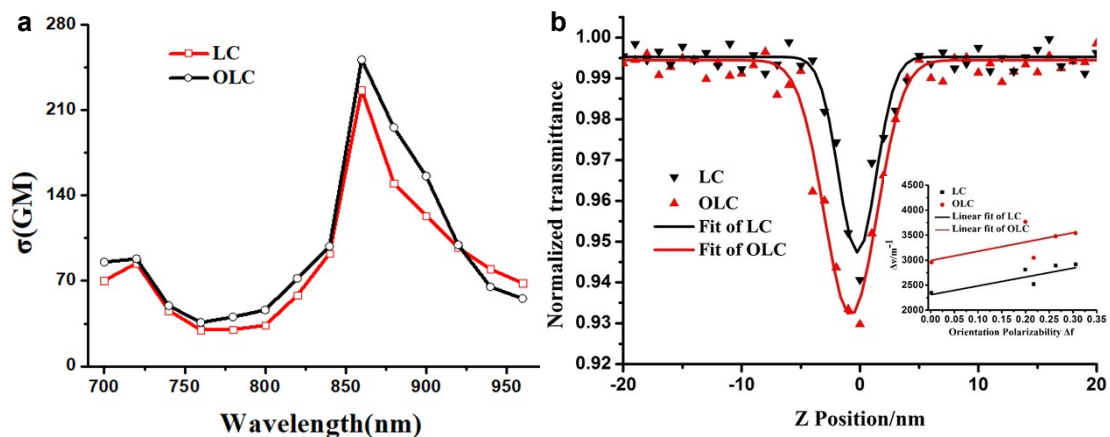


Fig. S5. (a) Two-photon cross-sections of **LC** and **OLC** in DMSO with $c = 0.8$ mM at the optimal excitation wavelength and (b) Nonlinear optical response of compounds **LC** and **OLC** in DMSO at 0.8 mM, obtained under an open aperture Z-scan at 860 nm. Inset: Lippert-Mataga plots for complex **LC** and **OLC**.

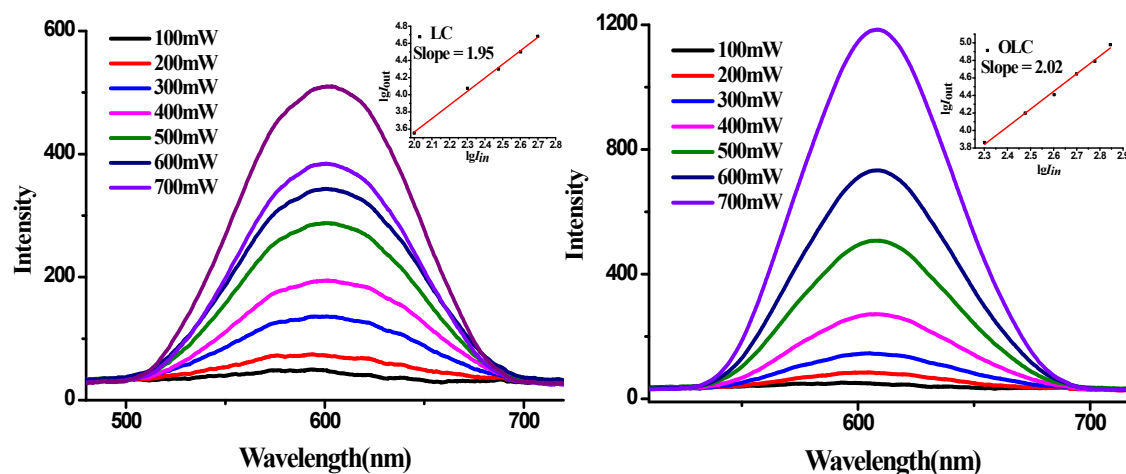


Fig. S6. Output fluorescence (I_0) vs. the square of input laser power (I_F)² at 860 nm for **LC** and **OLC**.

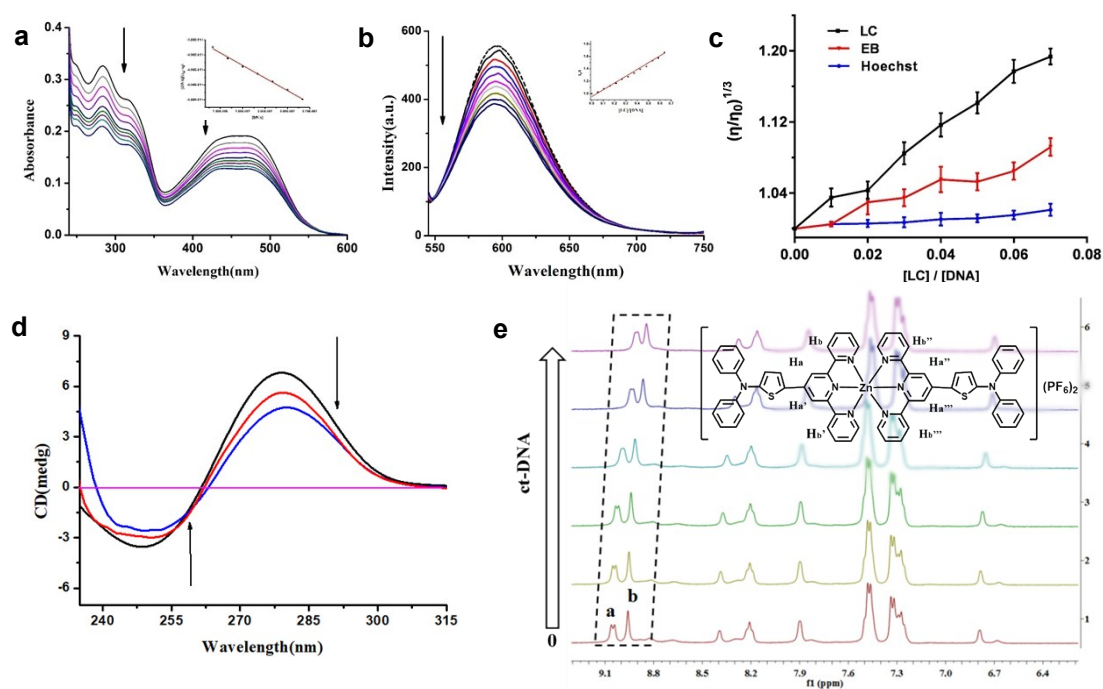


Fig. S7. (a) UV-*vis* absorption spectra of LC (2 μ M), in the absence and presence of increasing concentrations of ctDNA (0-0.45 μ M) in 50mM Tris-HCl buffer (pH=7.4, 50 mM NaCl). Inset: plots of $[DNA]/(\epsilon_a - \epsilon_f)$ vs. $[DNA]$ and the linear fit line. (b) Fluorescence spectra of EB bound to ctDNA in the presence of LC (0 - 6.4 μ M). $[EB] = 15 \mu$ M, $[DNA] = 15 \mu$ M. The arrows show the intensity changes upon increasing concentrations of the complex. Inset: fluorescence quenching curve of ctDNA-bound EB by LC. (c) The changes in the relative viscosities of ctDNA, EB and Hoechst with increasing concentrations of LC in buffer 50 mM NaCl. The total concentration of ctDNA is 50 μ M. (d) Circular dichroism spectra of ctDNA in the absence (DNA alone) and presence of LC. (e) 1H NMR spectral change of LC in the absence and presence of ctDNA in DMSO- d_6 solution.

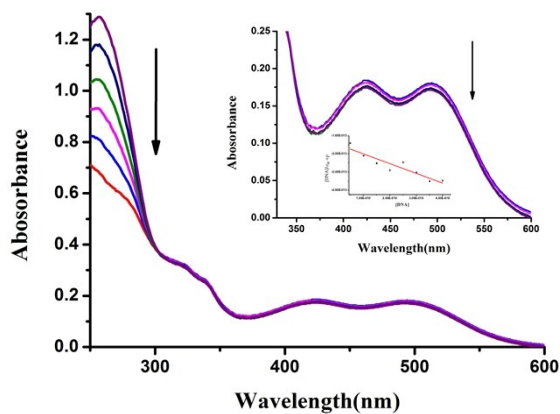


Fig. S8. UV-*vis* absorption spectra of **OLC** (2 μ M) in the absence and presence of increasing concentrations of ctDNA (0-0.45 μ M) in 50mM Tris-HCl buffer (pH = 7.4, 50 mM NaCl). Inset: plots of $[DNA]/(\epsilon_a - \epsilon_f)$ vs. $[DNA]$ and the linear fit line.

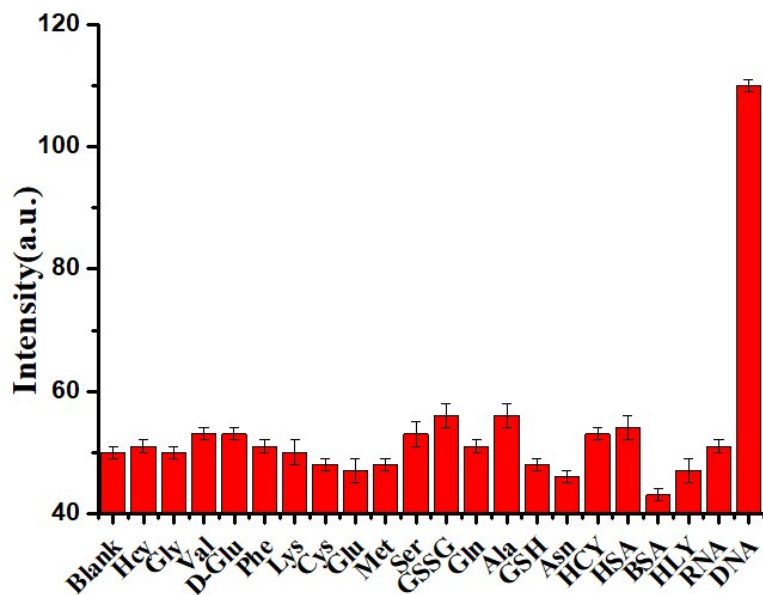


Fig. S9. Fluorescence intensity of **LC** (20 μ M), in the presence of various relevant analytes in Tris-HCl buffer (pH=7.4, 50 mM NaCl) at 37 $^{\circ}$ C.

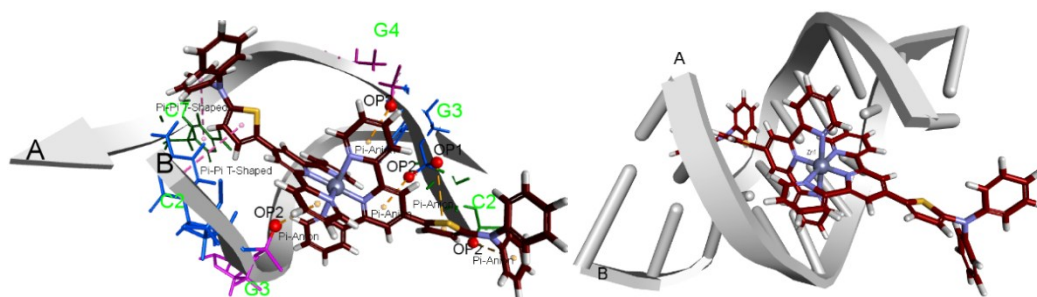


Fig. S10. Models obtained after molecular modeling of the interaction of **LC** with DNA (left) and RNA (right).

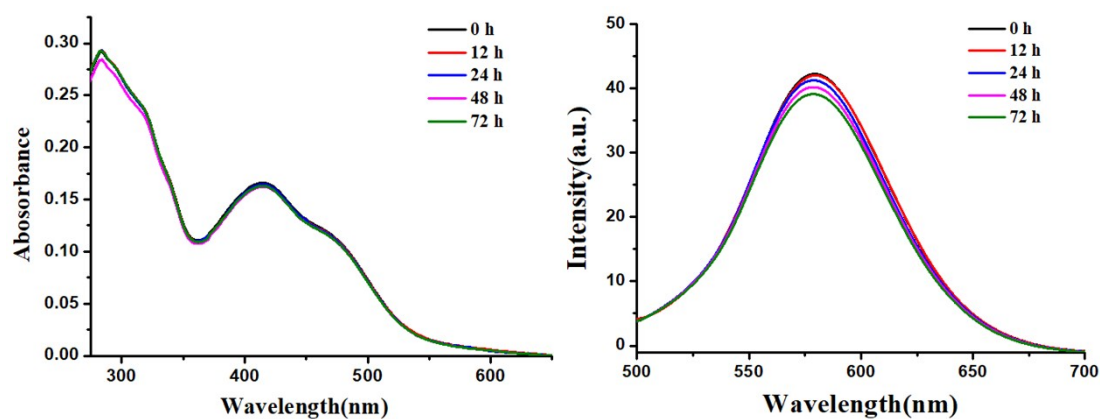


Fig. S11. Time evolution of UV-*vis* absorption spectra (left) and Fluorescence emission spectra

(right) of complex LC in PBS buffers.

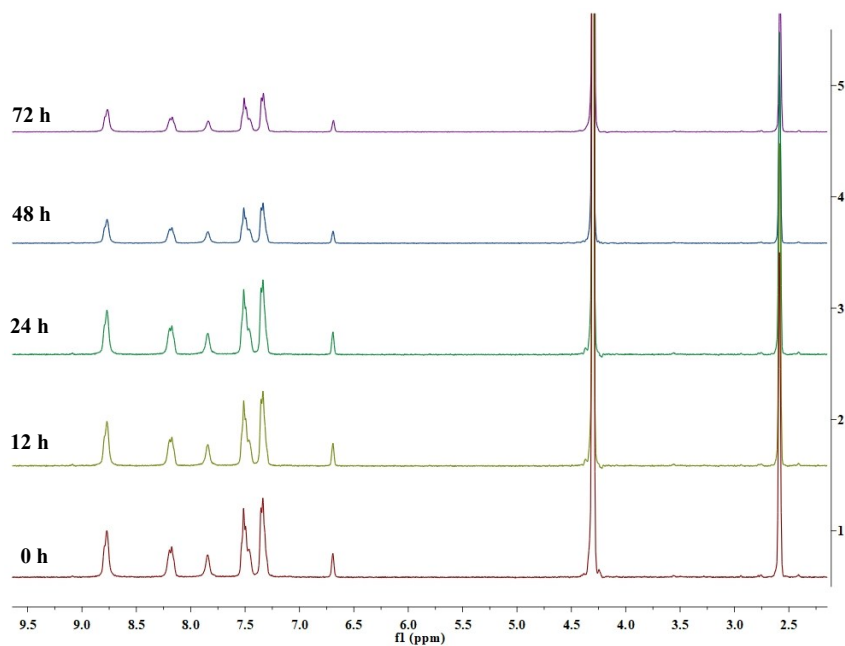


Fig. S12. The ¹H NMR spectra of complex LC in 90% D₂O/10% DMSO-d₆ at various time points.

The spectra were recorded at 300 K.

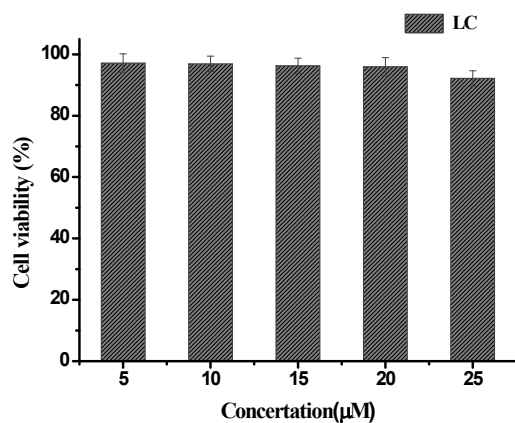


Fig. S13. Cytotoxicity data results obtained from the MTT assay.

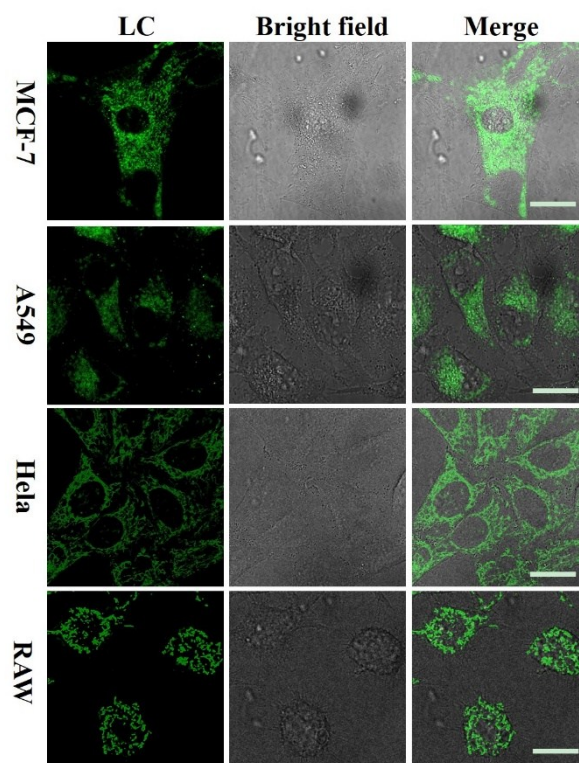


Fig. S14. Two-photon fluorescence images, Bright field images and Merge images of live MCF-7 cells, A549 cells, HeLa cells and RAW cells stained with LC (10 μ M, λ_{ex} = 840 nm, λ_{em} = 500-600 nm). Scale bar: 20 μ m.

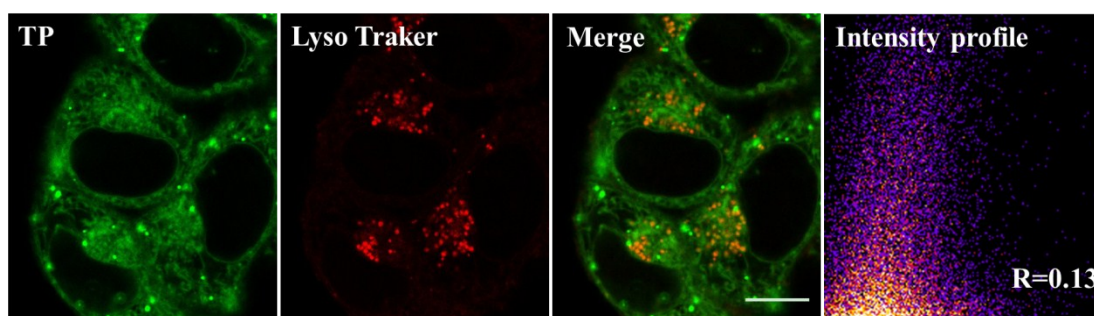


Fig. S15. Colocalization experiments involving LC (10 μ M) and Lyso Tracker in HepG2 cells. Scale bar: 20 μ m.

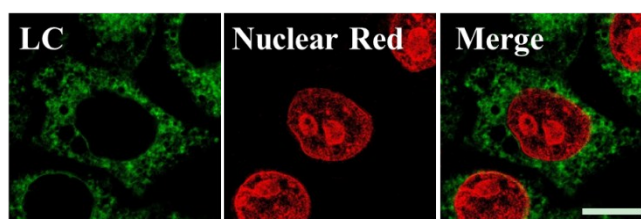


Fig. S16. HepG2 cells stained by complex LC after being fixed by paraformaldehyde. Scale bar: 20 μ m.

μm .

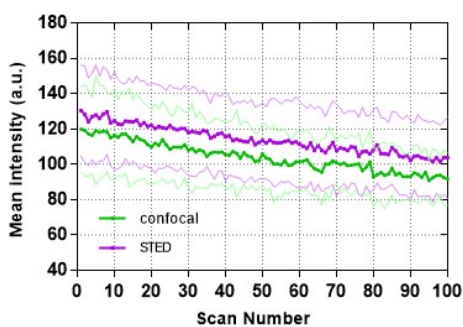


Fig. S17. Photo-stability of LC of confocal and STED imaging.

Table S1. Crystal data collection and structure refinement of LC

Empirical formula	$\text{C}_{62}\text{H}_{44}\text{N}_8\text{S}_2\text{ZnF}_{12}\text{P}_2$
Space group	$P2_1/n$
Formula weight	1338.50
CCDC	152166
Temperature	298(2) K
Wavelength	0.71069 Å
Crystal system, space group	Monoclinic, $P2_1/n$
Unit cell dimensions	$a = 21.356(5)\text{Å}$ $b = 13.467(5)\text{Å}$ $c = 22.171(5)\text{Å}$ $\beta = 110.931(5)^\circ$
Volume	$5956(3)\text{Å}^3$
Z, Calculated density	4, 1.493Mg/m ³
Absorption coefficient	0.624 mm ⁻¹
F(000)	2728
Crystal size	0.30 x 0.20 x 0.20 mm
Theta range for data collection	1.14 to 25.00
Limiting indices	$-25 \leq h \leq 25$, $-16 \leq k \leq 14$, $-26 \leq l \leq 26$
Completeness to theta = 25.00	99.9 %
Final R indices	$R_1 = 0.0742$, $wR_2 = 0.2590$

Table S2. Selected Bond Lengths (Å) and Bond Angles (°) of **LC**

Bond	Dist.	Bond	Dist.	Bond	Dist.
S(2)-C(13)	1.724(6)	Zn(1)-N(5)	2.210(5)	N(7)-C(25)	1.347(7)
Zn(1)-N(3)	2.082(4)	C(21)-C(7)	1.339(7)	P(1)-F(6)	1.576(7)
Zn(1)-N(7)	2.171(5)	C(16)-C(15)	1.363(8)	P(1)-F(3)	1.482(6)
Zn(1)-N(2)	2.201(5)	N(1)-C(49)	1.393(8)	P(2)-F(10)	1.521(6)
Zn(1)-N(4)	2.202(5)	C(20)-N(6)	1.347(7)	P(2)-F(12)	1.557(6)
Angle	(°)	Angle	(°)	Angle	(°)
F(8)-P(2)-F(12)	175.8(5)	N(6)-Zn(1)-N(3)	170.37(19)	C(6)-C(5)-N(8)	118.9(6)
F(10)-P(2)-F(7)	177.3(4)	N(6)-Zn(1)-N(7)	75.67(19)	C(4)-C(5)-N(8)	120.4(6)
N(3)-C(21)-C(22)	121.2(6)	N(3)-Zn(1)-N(2)	75.11(18)	C(4)-C(3)-C(2)	120.2(8)
C(49)-N(1)-C(55)	122.1(6)	N(6)-Zn(1)-N(5)	75.32(18)	C(1)-C(2)-C(3)	120.7(8)
C(11)-N(8)-C(5)	117.2(5)	N(2)-Zn(1)-N(5)	99.85(17)	C(5)-C(6)-C(1)	119.8(7)

Table S3. The photophysical data of complex **LC** and **OLC** in different solvents.

	Solvents	λ_{\max}^a (log ϵ_{\max}^b)	λ_{\max}^c	Φ^d	t / ns^e
LC	Benzene	279(6.48)	457	0.30	3.19
		399(2.94)			
		452(1.38)			
	Dichloromethane	281(6.22)	477	0.17	2.28
		412(1.91)			
		483(3.73)			
	Ethyl acetate	279(6.45)	466	0.29	2.14
		397(2.96)			
		453(1.97)			
	Acetonitrile	282(5.9)	505	0.028	2.06
		467(4.45)			
	Dimethyl sulfoxide	281(6.45)	501	0.14	2.11
408(3.06)					
453(2.27)					
DMSO: H ₂ O =1:1	284(5.84)	555	0.0031	0.86	
	468(5.11)				
OLC	Benzene	276(5.36)	498	0.29	3.26
		417(3.46)			

Dichloromethane	317(3.59)	522	0.11	3.76
	422(1.94)			
	511(3.71)			
Ethyl acetate	281(5.16)	508	0.29	3.45
	410(3.26)			
	467(2.04)			
Acetonitrile	329(3.91)	539	0.012	2.71
	488(5.35)			
Dimethyl sulfoxide	284(5.17)	536	0.068	3.09
	421(3.18)			
	480(2.77)			
DMSO: H ₂ O =1:1	284(4.44)	575	0.0011	0.86
	483(5.16)			

^a Peak position of the longest absorption band in nm.

^b Maximum molar extinction coefficient.

^c Peak position of SPEF, excited at the maximum wavelength of absorption.

^d Fluorescence quantum yield.

^e Fluorescence lifetime(ns).

Table S4. Two photon absorption data for **LC** and **OLC**

Complex	λ^a (nm)	β^b (cm/GM)	σ^c (GM)
LC	860	0.0057	2268.75
OLC	860	0.0062	2418.29

^a Maximum nonlinear absorption wavelength.

^b Two photon absorption coefficient.

^c Two photon absorption cross-section.

Table S5. Calculated linear absorption properties (nm), excitation energy (eV), oscillator strengths and major contribution for **LC** and **OLC**.

Complex	ΔE_i^a	λ [nm] ^b	Oscillator strengths	Nature of the transition
LC	2.70	458	0.0253	323(H-4) \rightarrow 329(L+3)(0.57)
	3.02	409	0.0453	324(H-3) \rightarrow 333(L+5)(0.70)

OLC	2.53	488	0.0049	373(H-2) → 379(L+3)(0.66)
	2.90	426	0.0306	372(H-3) → 380(L+4)(0.69)

^a The energy gap of the single-photon absorption band.

^b Peak position of the maximum absorption band.

References

1. H. Wang, Q. Zhang, J. Zhang, L. Li, Q. Zhang, S. L. Li, S. Y. Zhang, J. Y. Wu and Y. P. Tian, *Dyes. Pigm.*, 2014, **102**, 263-272.
2. S. A. Patel, M. Cozzuol, J. M. Hales, C. I. Richards, M. Sartin, J. C. Hsiang, T. Vosch, J. W. Perry and R. M. Dickson, *J. Phys. Chem. C.*, 2009, **113**, 20264-20270.
3. Z. Zheng, Q. Zhang, Z. P. Yu, M. D. Yang, H. P. Zhou, J. Y. Wu and Y. P. Tian, *J. Mater. Chem. C.*, 2013, **1**, 822-830.
4. C. Xu and W. W. Webb, *J. Opt. Soc. Am. B.*, 1996, **13**, 481-491.
5. M. A. Albota, C. Xu and W. W. Webb, *Appl. Opt.*, 1998, **37**, 7352-7356.
6. Y. Q. Liu, H. Wang, J. Zhang, S. L. Li, C. K. Wang, H. J. Ding, J. Y. Wu and Y. P. Tian, *Optical Materials.*, 2014, **36**, 687-696.
7. S. M. Ji, J. Yang, Q. Yang, S. S. Liu, M. D. Chen and J. Z. Zhao, *J. Org. Chem.*, 2009, **74**, 4855-4865.
8. F. S. Shen, Z. P. Luo, H. H. Liu, R. Wang, S. L. Zhang, J. H. Gan and J. Sheng, *Nucleic. Acids. Res.*, 2017, **45**, 3537-3546.
9. X. H. Tian, Y. Z. Zhu, M. Z. Zhang, J. Y. Tan, Q. Zhang, X. Y. Wang, J. X. Yang, H. P. Zhou, J. Y. Wu and Y. P. Tian, *Dyes. Pigm.*, 2017, **139**, 431-439.